JACS
JOURNAL OF THE AMERICAN CHEMICAL SOCIETY

ARTICLE

pubs.acs.org/JACS

Structural Defects in Periodic and Quasicrystalline Binary Nanocrystal Superlattices

Maryna I. Bodnarchuk,[†] Elena V. Shevchenko,[‡] and Dmitri V. Talapin*[,†,‡]

[†]Department of Chemistry and James Frank Institute, University of Chicago, Chicago, Illinois 60637, United States

[‡]Center for Nanoscale Materials, Argonne National Lab, Argonne, Illinois 60439, United States

Supporting Information

ABSTRACT: Binary nanocrystal superlattices (BNSLs) emerge as an important class of man-made materials where components and functionalities can be added, tuned, or combined in a predictable manner. These amazingly complex structures spontaneously self-assemble from colloidal solutions containing binary mixtures of functional (semiconducting, magnetic, plasmonic, etc.) nanocrystals. Further developments of the BNSL-based materials require a deep understanding and control over BNSL formation and structural perfection. Like any solid, BNSL can contain different kinds of structural defects. It is well-known that defects can have a tremendous effect on the material's behavior. Defect engineering is used to modify and improve many of the mechanical, electrical, magnetic, and optical properties of conventional solids. In this work, we provide the first systematic analysis of structural defects in various BNSL structures. We used BNSLs as a platform for studying structural defects in both periodic (crystalline) and aperiodic (quasicrystalline) lattices, as well as for direct imaging of the interfaces between crystalline and quasicrystalline domains. Such direct observation of local imperfections in complex multicomponent lattices provides a unique insight into the fundamental aspects of crystal formation.

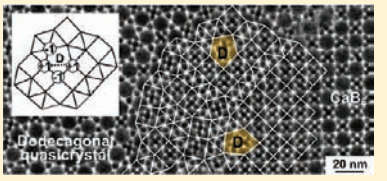

1. INTRODUCTION

The colloidal synthesis of inorganic nanocrystals (NCs) experienced great success in the past decade, providing researchers with scalable quantities of highly monodisperse and regularly shaped metallic, semiconducting, and magnetic NCs.[1−3] These NCs are now extensively studied as the building blocks of novel functional solids for the next generations of optical and electronic devices. Just like atoms in conventional solids, highly uniform NCs can be used as "designer atoms" to construct various long-range ordered superstructures (superlattices) with properties defined by tuning NC size, shape, and chemical composition as well as by controlling the arrangements of individual NCs inside superlattices. These new man-made materials provide a powerful platform for designing programmable solids with tailored electronic, magnetic, and optical properties.

Depending on the number of NC components integrated into a superlattice, one can distinguish between single-component NC superlattices,[2,4,5] binary NC superlattices (BNSLs),[6−10] and even ternary NC superlattices (TNSLs).[11,12] Single component NC superlattices form *fcc*, *hcp*, simple hexagonal, and *bcc* structures well-known in atomic solids.[2,4,13] BNSLs and TNSLs demonstrated amazing structural complexity, with more than a dozen reported structures that often had analogues among known ionic and intermetallic compounds.[7,11,14] Furthermore, BNSLs can exhibit aperiodic dodecagonal quasicrystalline ordering with "forbidden" 12-fold rotational symmetry.[15] The mechanism for the nucleation and growth of NC superlattices depends on the conditions of colloidal destabilization. For example, fast evaporation of solvent can result in the nucleation and lateral growth of superlattices at the liquid−air interface,[5,16,17] whereas slow diffusion of nonsolvent into a colloidal solution of NCs leads to the nucleation and growth of superlattices at the substrate−liquid interface.[18]

The ability to form complex structures via spontaneous self-organization is a fascinating property of colloidal NCs which requires detailed investigations. Current research efforts are primarily focused on obtaining macroscopically large superlattices, either in the form of thin films[7,8,11] or as three-dimensional colloidal crystals.[2,19−22] Despite obvious progress in structural characterization of BNSLs and TNSLs using transmission electron microscopy (TEM) and electron tomography,[17,23] relatively little is known about structural defects in multicomponent NC superlattices. Here we show that BNSLs represent a very convenient model system for studying defects in complex multicomponent lattices. In contrast to perfect lattices which can be analyzed in the reciprocal space by diffraction techniques, the analysis of local distortions of crystal lattice requires precise real-space imaging. It is a challenging task for atomic lattices, especially when it comes to analysis of three dimensional objects. Colloidal particles (NCs, latex beads, etc.) allow modeling the behaviors of atomic systems on a much larger scale. For example, micrometer size colloids were used for direct optical imaging of dislocation nucleation[24] and dislocation dynamics[25] in *fcc* lattices. TEM imaging was also used to analyze structural defects in the *fcc* superlattices of Au and Ag NCs.[26] In this work we focus on

Received: July 30, 2011
Published: October 18, 2011

structural imperfections in BNSLs. We found that BNSLs can be used as a convenient platform for studying various point defects, linear defects, and planar defects in complex multicomponent lattices. Very rich BNSL phase diagrams allow studying defects in cubic, hexagonal, tetragonal, and quasicrystalline lattices. Moreover, TEM imaging can be used for the real-space analysis of grain boundaries and interfaces between different structures, including very intriguing interfaces between periodic and aperiodic (quasicrystalline) BNSLs. To collect statistically relevant information, we analyzed TEM images from about 500 samples representing 15 BNSL types. These BNSLs self-assembled from different combinations of semiconductor (CdSe, PbS, PbSe), metallic (Au, Pd, Ag), and magnetic (Fe_2O_3, $CoFe_2O_4$) NCs.

2. EXPERIMENTAL SECTION

2.1. Nanocrystal Synthesis. *Synthesis of PbS NCs* capped with oleic acid was performed from lead oleate and bis(trimethylsilyl)sulfide according to ref 27. *PbSe NCs* stabilized with oleic acid were synthesized from lead oleate and trioctylphosphine selenide (TOPSe). The details of preparation can be found in ref 28. *CdSe NCs* were synthesized in a hexadecylamine/trioctylphosphine oxide/trioctylphospine mixture using dimethylcadmium and TOPSe according to ref 29. The *synthesis of $CoFe_2O_4$ NCs* was carried out by high-temperature decomposition of mixed iron(III)/cobalt(II) oleate at 320 °C in the presence of oleic acid as the stabilizing agent.[30] The synthesis of *Fe_3O_4 NCs* was carried out from iron oleate in the presence of oleic acid according to ref 31. Dodecanethiol-stabilized 5.2 nm *Au NCs* were synthesized as described in ref 32. Oleylamine-stabilized 3.8 nm *Au NCs* were synthesized as described in ref 33. Dodecanethiol-stabilized 3.4 nm *Pd NCs* were synthesized as described in ref 14.

2.2. Preparation of Binary Nanocrystal Superlattices. Carbon-coated TEM grids (type-B, Ted Pella) were used as substrates for nanocrystal self-assembly. Protective Formvar coating of grids was removed by dipping the grids in toluene for 15−20 s followed by drying on filter paper. The grids were placed into the tilted glass vial, and ∼20−25 μL of the solution containing a mixture of two types of NCs with desired size and concentration ratios was placed above the grid. Various alkanes, tetrachloroethylene, chlorobenzene, and toluene, were used as solvents for NCs. Different temperatures in the range of −20 to 100 °C were used for drying of the solutions.[34] The solutions were evaporated under vacuum or nitrogen flow as was described previously in ref 34.

2.3. Structural Characterization of Binary Superlattices. Transmission electron microscopy (TEM) images and electron diffraction patterns were obtained using an FEI Technai F3 microscope operating at the acceleration voltage of 300 kV. All TEM images were taken on three-dimensional BNSLs. TEM imaging of thick NC layers was generally difficult because of strong electron absorption. We therefore imaged BNSL domains containing 3−5 unit cells in thickness that accurately represented three-dimensional lattices. The TEM images were compared to the BNSL projections simulated using Crystal Maker 1.4 software package.

3. RESULTS AND DISCUSSION

General Remarks: BNSLs versus Conventional Solids and Micrometer-Size Colloidal Particles. BNSLs represent an interesting and in many aspects unique example of self-assembling systems. They naturally occupy a niche between atomic solids and colloidal crystals formed by micrometer-size plastic or silica beads.[35] In contrast to atoms, which have fixed dimensions, the size of NCs can be precisely tuned in a broad range. As a result, different BNSL structures can be obtained from NC pairs with the same chemical composition but with different NC size ratios. The NC size ratio is often called γ-ratio ($\gamma = d_{small}/d_{large}$). This parameter should be calculated using the actual NC size estimated as $d_{NC} = d_{core} + 2h_{shell}$, where d_{core} is the diameter of the inorganic NC core and h_{shell} is the effective thickness of ligand shells measured for different NC−ligand pairs.[14]

Table 1. Classification of Defects Observed in BNSLs Based on the Defect Dimensionality

defect type	characteristic examples
point defects (zero-dimensional defects)	vacancy
	interstitial NC
	substitutional NC
line defects (one-dimensional defects)	edge dislocation
	screw dislocation
	disclination
planar defects (two-dimensional defects)	*External*
	free surface
	Internal
	grain boundary
	antiphase boundary
	twin boundary
	stacking fault
	phase boundary
volume defects (three-dimensional defects)	void
	crack
	precipitate

Different from atoms and ions, NCs cannot be considered identical to each other and possess some size and shape distributions. The distribution of NC sizes can build local strains and induce the formation of conventional structural defects or even create new types of defects discussed in Section 3.6. NCs can interact with each other through complex interparticle potentials induced by van der Waals,[36] electrostatic (Coulombic[14] and dipolar[13]), and in certain cases magnetic[37] forces. As a result, BNSLs exhibit amazingly sophisticated structures that are closer in complexity to atomic solids rather than to assemblies of micrometer-sized colloidal particles. Such complexity results in our currently limited understanding of the thermodynamics and kinetics associated with self-assembly of NCs into BNSLs. Recent studies suggested that both enthalpic and entropic factors contribute with similar weights to the changes in free energy during the assembly process.[34]

3.1. Classification of Defects in BNSLs. The defects observed in BNSLs can be classified into four main classes based on the defect dimensionality (Table 1):

(i) Point defects or zero-dimensional defects are formed by one missing NC or by irregular placement of one NC in otherwise perfect BNSL structure. Point defects include vacancies, interstitial NCs, and substitutional NCs. Depending on the nature of interstitial or substitutional sites, one can distinguish between self-interstitial (self-substitutional) and impurity-interstitial (impurity-substitutional) defects. In the former case, the defect is formed by one of the two NC types forming a regular BNSL lattice, while in the latter case the defects are formed by the impurity NCs.

(ii) Line defects or one-dimensional defects are formed by one line or several lines of NCs that do not follow

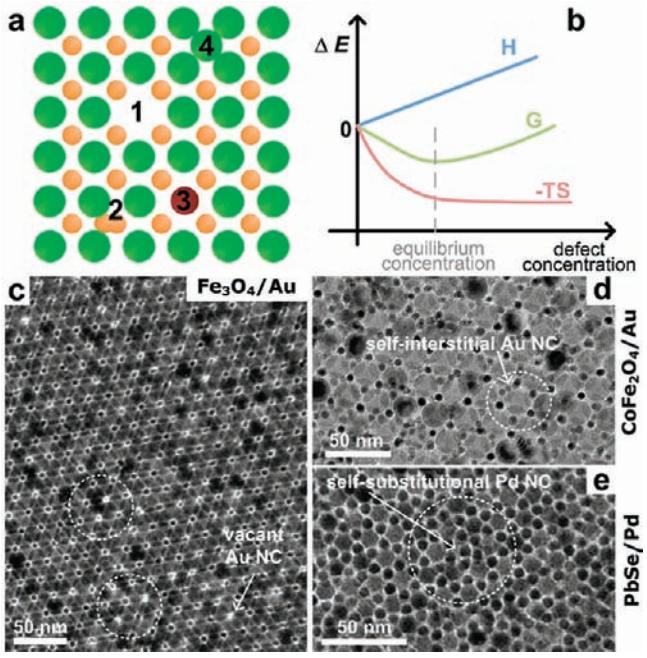

Figure 1. (a) Schematic illustration of typical point defects in BNSLs: 1, vacancy; 2, self-interstitial NC; 3, impurity substitutional NC; 4, self-substitutional NC. (b) Dependence of the Gibbs free energy of crystal on the concentration of point defects. (c–e) TEM images of BNSLs with various point defects: (c) vacancies and divacancies of Au NCs in the NaCl-type binary superlattice assembled from 15 nm Fe_3O_4 and 5.2 nm Au NCs; (d) self-interstitial Au NCs in NaCl-type BNSL self-assembled from 20 nm $CoFe_2O_4$ and 5 nm Au NCs; (e) self-substitutional Pd NC in an AlB_2-type binary superlattice from 7.7 nm PbSe NCs and 4.9 nm Pd NCs.

translational or rotational symmetry of BNSL. Line defects include dislocations and disclinations.

(iii) Planar defects or two-dimensional defects represent interfaces between BNSL domains. These defects include grain boundaries, twin boundaries, stacking faults, phase boundaries, antiphase boundaries, etc.

(iv) Volume defects or three-dimensional defects include voids, precipitates, and cracks in BNSL lattices.

3.2. Point (Zero-Dimensional) Defects. These are by far the most common defects in BNSLs. Typical point defects are schematically shown in Figure 1a. In contrast to other structural imperfections, point defects are always present in solids as a consequence of the natural tendency toward disorder. The presence of vacancies and other point defects increases enthalpy of the crystal due to the additional energy required to break bonds and accommodate strain. The linear dependence of enthalpy on the defect concentration provides a good statistical approximation for any type of noninteracting point defects. At the same time, point defects increase configurational entropy of the crystal (Figure 1b). As a result, free energy reaches its minimum at a certain (nonzero at finite temperature) concentration of point defects corresponding to the equilibrium state. The equilibrium concentration of vacancies can be expressed as $N_V/N = \exp(-Q/k_BT)$, where N_V is the number of vacancies; N is the total number of lattice sites; Q is the vacancy formation energy; k_B is Boltzmann's constant; and T is the temperature. The above equation, however, does not account for the kinetic factors which are often responsible for nonequilibrium point defects introduced during crystal growth.[38]

Figure 1c shows the examples of vacancies in the NaCl-type BNSL self-assembled from Fe_3O_4 and Au NCs. The other examples of vacancies in different BNSL types are shown in Figure S1 (Supporting Information). A survey of multiple samples suggested that the concentration of vacancies is higher in BNSLs with a large difference in sizes of small and large NCs. We typically observed vacancies in BNSLs with $\gamma < 0.5$, i.e., in the range of stability for NaCl and CaB_6-type lattices. These structures typically were missing small NCs, which did not cause significant lattice distortions. In addition to individual vacancies, we often observed the vacancy pairs, such as those highlighted in Figure 1c. Such vacancy pairs form so-called divacancy defects. For example, divacancies form in metal halides under the effect of ionizing irradiation.[39] In conventional *fcc* crystals, there is an attraction between individual vacancy sites, resulting in positive divacancy binding energy.[40]

Interstitial NCs represent another rather common point defect in BNSLs. These defects were found in BNSLs at lower concentrations compared to vacancies because interstitial NCs cause local lattice expansion that displaces many NCs and costs more energy compared to the energy associated with the vacancy formation. In common solids, the interstitial atom costs roughly three times the vacancy formation energy.[41] Similar to the vacancies, interstitial NCs were typically observed in the BNSLs with small γ-ratio where a small NC could fit into empty interstitial site without introducing significant expansion of the unit cell. This effect is demonstrated in Figure 1d for NaCl-type BNSL self-assembled from 20 nm $CoFe_2O_4$ NCs and ~5 nm Au NCs ($\gamma \sim 0.29$). In this structure, large $CoFe_2O_4$ NCs form an *fcc* sublattice where Au NCs occupy the octahedral voids. NaCl-type structure also contains empty tetrahedral interstitial sites which could accommodate NCs with size smaller than 22% the size of $CoFe_2O_4$ NCs (i.e., ~4.7 nm with the ligand shell). Indeed, we found multiple examples of interstitial Au NCs occupying the tetrahedral interstitial sites. Interestingly, the average size of interstitial Au NCs was smaller than the average size of Au NCs occupying the lattice sites (Figure 1d). Such size selection between NC occupying the lattice sites and interstitial sites allowed minimization of the lattice strain. This type of size selection is not possible in conventional solids where atomic radii cannot be "tuned" without changing their chemical nature. In fact, the possibility of discrimination between lattice and defect NCs based on the small difference in NC size washes out the distinction between self-interstitial and impurity-interstitial defects in BNSLs.

In BNSLs it is also rather common to observe self-substitutional NCs. In this point defect, the NC occupies the site belonging to a different sublattice. For example, Figure 1e shows the [001] projection of AlB_2-type BNSL self-assembled from 7.7 nm PbSe and 4.9 nm Pd NCs ($\gamma = 0.74$) where one Pd NC occupies the lattice site belonging to the sublattice formed by PbSe NCs. Self-substitutional NCs are more common in BNSLs with large γ-ratio where self-substitution does not introduce large lattice strain. In BNSLs with small γ-ratio, several small NCs can occupy the same site from the sublattice of large NCs. An example of such multisubstitution where two 5 nm Au NCs occupied the site of 11 nm $CoFe_2O_4$ NCs in AlB_2-type BNSL is shown in Figure S1 (Supporting Information).

3.3. Line (One-Dimensional) Defects. Dislocations and disclinations are examples of line defects. In three-dimensional crystals, these defects result in the violation of translational or rotational symmetry along a straight line. Both dislocations and disclinations can be found in TEM images of BNSL projections.

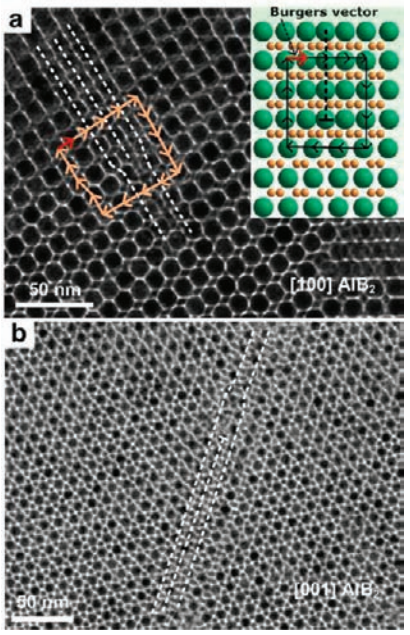

Figure 2. (a) Edge dislocation observed in the [100] projection of AlB_2-type BNSL self-assembled from 11 nm $CoFe_2O_4$ and 4 nm PbSe nanocrystals. The inset shows a model of dislocation in AlB_2-type BNSL with Burgers circuit and Burgers vector. (b) TEM image of [001] projection for AlB_2-type BNSL self-assembled from 7.7 nm PbSe and 3.4 nm Pd NCs. The dislocation line is perpendicular to the plane of the figure and highlighted (⊥).

3.3.1. Dislocations. Dislocation is a line of crystal lattice misalignment. Dislocations provide the most important mechanism by which traditional solids can be deformed, and they also can play an important role in crystal growth.[42] In crystallography, dislocations are characterized by the Burgers vector that represents the magnitude and direction of the lattice distortion. The Burgers vector can be defined by drawing a circuit around the dislocation on any surface which intersects the dislocation. For example, the inset in Figure 2a shows a rectangle drawn around the dislocation by counting four unit cells along each direction. In an ideal lattice, such an operation should form a closed loop, but the presence of a dislocation results in the lattice distortion. The vector that closes this loop is the Burgers vector. The magnitude of the Burgers vector (b) is related to the dislocation energy per unit length as $E_{disl} \approx Gb^2$, where G is the shear modulus.[42]

There are two main types of dislocations: edge dislocation and screw dislocation. An edge dislocation forms by inserting an extra plain of NCs that goes only part of the way through a BNSL (so-called half-plane), and the Burgers vector is perpendicular to the dislocation line. Two examples of edge dislocations in AlB_2-type BNSLs are shown in Figure 2. In Figure 2a the dislocation line is normal to [100] projection of the AlB_2 lattice; the TEM image is in a good agreement with its model shown as the inset. Figure 2b shows the dislocation along the ⟨001⟩ axis of AlB_2-type BNSL. Edge dislocations can be found in different BNSL structures. For example, Figure S2 (Supporting Information) shows the edge dislocation normal to the [100] projection of $NaZn_{13}$-type BNSL assembled of 8.1 nm CdSe and 4 nm Ag NCs. The lattice planes bend around the edge of the terminating plane resulting in the perfectly ordered BNSL structure on either side of the edge dislocation.

For screw dislocations, the Burgers vector is parallel to the dislocation line, and this type of defect is difficult to recognize in two-dimensional BNSL projections. At the same time, there are numerous examples of screw dislocations observed in the high-resolution SEM images of the surface of *fcc* NC superlattices (Figure S3, Supporting Information). In addition to the cases described above, one should expect the existence of mixed dislocations for which the Burgers vector has an arbitrary angle with respect to the dislocation line.[42]

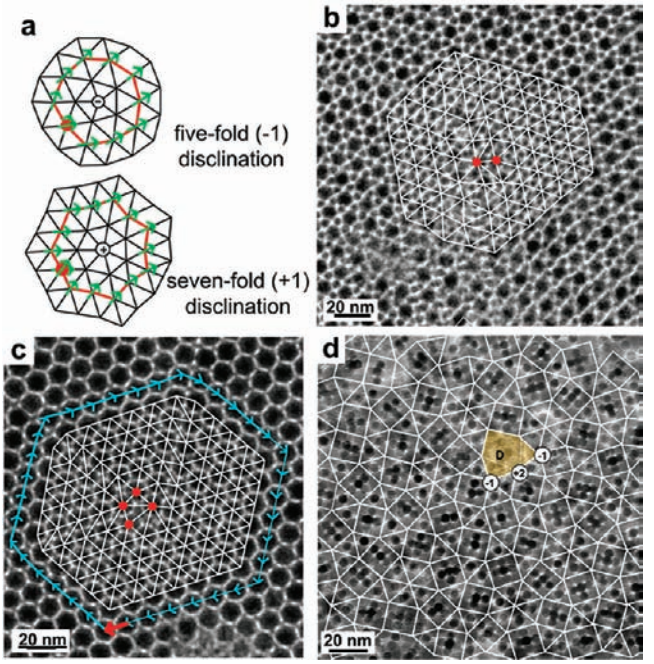

Figure 3. (a) Schematic illustration of 5-fold (−1) and 7-fold (+1) disclinations in a hexagonal lattice (adopted from ref 43). (b) TEM image of [001] projection for AlB_2-type BNSL self-assembled from 7.7 nm PbSe and 3.4 nm Pd NCs with a tightly bound pair of 5-fold and 7-fold disclinations. (c) TEM image of [001] projection for AlB_2-type BNSL self-assembled from 11 nm $CoFe_2O_4$ and 4 nm PbSe NCs with two pairs of disclinations of opposite sign. Blue arrows show the Burgers circuit around the disclinations pair. The red arrow is the Burgers vector characteristic of the dislocation. (d) TEM image of dodecagonal quasicrystalline superlattice self-assembled from 13.4 nm Fe_2O_3 and 5 nm Au NCs with several disclination points (see text for details).

3.3.2. Disclinations. Disclination is the line defect where rotational symmetry is violated. The disclination can be viewed as an insertion or removal of a wedge of material into (from) the lattice. Disclinations can be characterized by the disclination strength, that is, the amount by which a vector aligned along one of the lattice directions is rotated upon "parallel transport" along a closed path around the declination (Figure 3a).[43] For example, in crystals with hexagonal symmetry the disclination strength is defined in units of 60° ($\pi/6$) which is the smallest rotation angle allowed in these periodic lattices. The sign of the disclination determines the same (+) or the opposite (−) direction of vector rotation with respect to the direction of parallel transport.[43] In a simple triangular lattice, a +1 disclination corresponds to a point with 7-fold symmetry, whereas −1 disclination corresponds to a point with 5-fold symmetry (Figure 3a).

In BNSLs, disclinations often form tightly bound pairs of disclinations of opposite signs. Thus, in TEM images of AlB_2-type BNSLs (Figures 3b and 3c), one can find both lattice sites surrounded by seven large NC neighbors and sites with five large NC neighbors, which are the 7-fold (+1) and 5-fold (−1) wedge

disclinations, respectively. Such disclinations are terminated by the stacking faults as one can see in the TEM images. The disclination pairs with opposite sign exclude or compensate each other restoring the long-range order of the crystalline lattice.[44] At the same time, the presence of one or several bound pairs of disclinations locally disrupts the translational order of the BNSL lattice, introducing a dislocation with Burgers vector normal to the disclination lines as shown in Figure 3c.

3.3.3. Line Defects in Quasicrystalline BNSLs. In addition to different crystalline phases, BNSLs often form quasicrystals that demonstrate long-range order without any translational symmetry.[15] Quasicrystalline superlattices often exhibit symmetry elements forbidden in periodic structures. We have recently demonstrated that different combinations of dielectric (e.g., Fe_2O_3, PbS) and metallic (Au, Ag, Pd) NCs with $\gamma \approx 0.43$ can self-assemble into binary superlattices with long-range quasicrystalline order.[15] At this γ-ratio the packing densities of AlB_2- and CaB_6-type BNSLs are equal to each other (~0.70), and both structures can form simultaneously.[15] Under these circumstances, cocrystallization of AlB_2- and CaB_6-type BNSLs resulted in the formation of a dodecagonal quasicrystalline (DDQC) phase with 12-fold rotational symmetry and irrational stoichiometry $A_{(2+\sqrt{3})}B_{(4+6\sqrt{3})} \sim AB_{3.86}$ (Figure 3d). The emergence of quasi-periodicity was explained as a result of maximizing the configurational entropy for arrangement of square and triangular "tiles".[45,46] The analysis of structural defects in quasicrystals requires different approaches because disruption of the periodicity, which defines defects in solids, does not apply to aperiodic structures. To analyze DDQC superlattices we projected them onto a square-triangular tiling as shown in Figure 3d. Square "tiles" represented the unit cells of the CaB_6-type lattice, while triangular "tiles" were structurally identical to the half-unit cells of the AlB_2 lattice.[15] Leung et al. studied theoretically the topological defects in aperiodic square-triangular tilings and introduced definitions of disclinations and dislocations in these structures.[47] The disclination strength for defects in DDQC superlattices can be calculated by counting the numbers of square and triangular "tiles" with a shared vertex (Figure 3d). The disclination strength is then calculated as $n = 12(n_{sq}/4 + n_{tr}/6 - 1)$, where n_{sq} and n_{tr} are the numbers of squares and triangle, respectively.[47] A dislocation can be defined as a neighboring pair or cluster of disclinations with equal and opposite strengths.[47] Figure 3d shows such groups of disclinations of opposite strength in the DDQC superlattice self-assembled from 13.4 nm Fe_2O_3 and 5 nm Au NCs. The discussion of the DDQC superlattices will be continued in Section 3.4.6.

3.4. Planar (Two-Dimensional) Defects. Planar defects in BNSLs can be subdivided into external and internal. External or free surface defects are represented by surface terminations and reconstructions, while the internal planar defects include stacking faults, twin boundaries, antiphase boundaries, grain boundaries, and phase boundaries (Table 1). This work focuses on the internal structural features observed in BNSLs.

3.4.1. Stacking Faults. In atomic solids, a stacking fault is a disruption in the stacking sequence of atomic planes. A simple example of stacking faults can be found in the *fcc* lattice where the stacking sequence of the (111) planes should be ABCABCABC. Any change of this sequence results in a stacking fault. Stacking faults are common in atomic solids; we also often observed them in BNSLs with AlB_2-type structure. Figure 4a shows a model of a typically observed stacking fault in BNSLs where the stacking sequence along the {110} direction of the AlB_2 lattice is

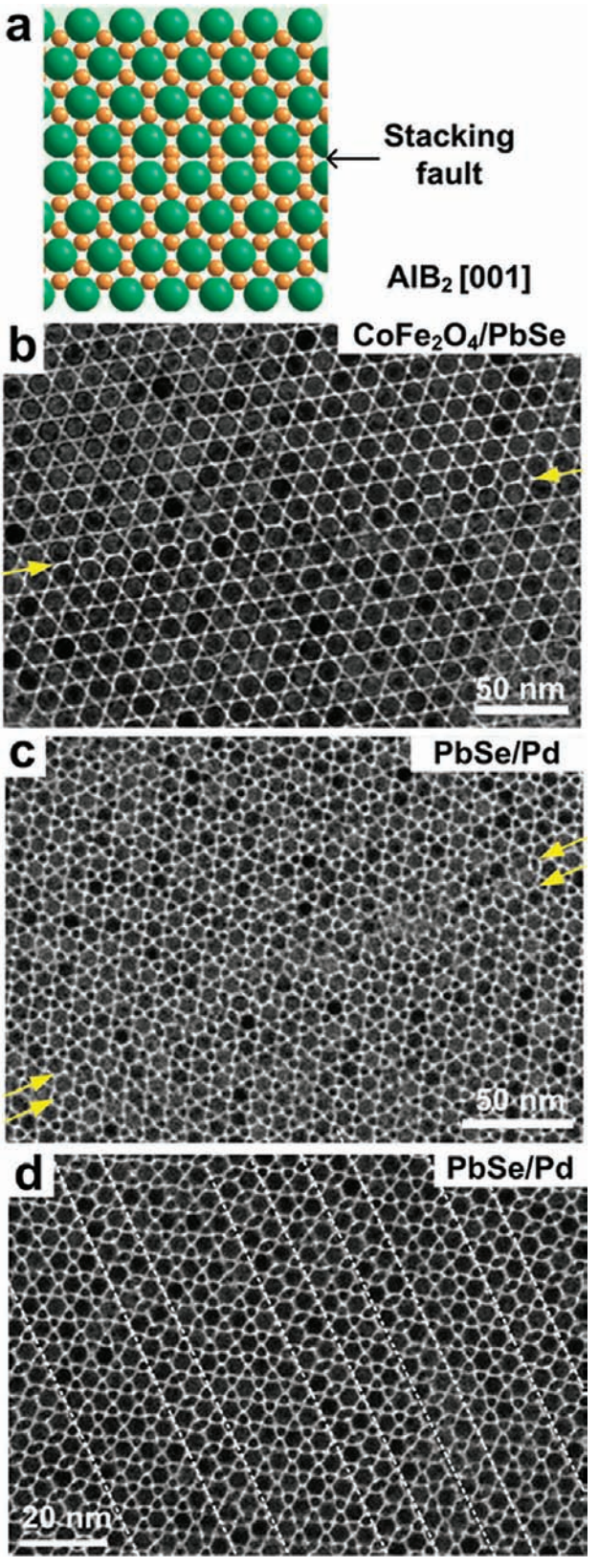

Figure 4. Stacking faults in BNSLs. (a) Model of a stacking fault viewed along the {100} direction of the AlB_2 lattice. (b) TEM image showing the [001] projection of the AlB_2-type BNSL self-assembled from 11 nm $CoFe_2O_4$ and 4 nm PbSe NCs. The stacking fault is highlighted by yellow arrows. (c) Stacking fault pairs observed in BNSL assembled from 7.7 nm PbSe and 3.4 nm Pd NCs. (d) Multiple stacking faults in PbSe/Pd BNSL.

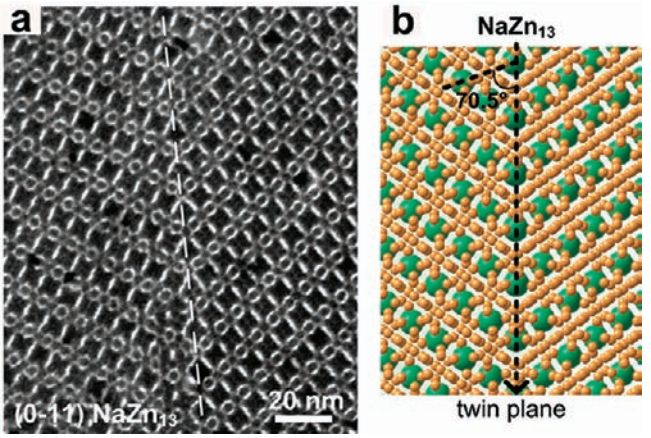

Figure 5. (a) TEM image and (b) model of twinned BNSL isostructural with the $NaZn_{13}$ lattice viewed along the [0-11] projection. The BNSL self-assembled from 5.8 nm PbSe NCs and 3.0 nm Pd NCs.

interrupted by removing one layer of large NCs (e.g., Figure 4b). At the same time, we noticed that many stacking faults observed in AlB_2-type BNSLs had a more complex structure which can be described as two stacking faults separated by one unit cell (Figure 4c and S4, Supporting Information). We can speculate that this double-fault defect has lower energy than the individual stacking fault. Some BNSL domains showed multiple stacking faults along the {100} direction of the AlB_2 lattice (Figure 4d). The stacking faults were bordered by either the edges of superlattice domain or by the edge dislocations as shown in Figure S4 (Supporting Information). The presence of stacking faults did not introduce significant distortions to the long-range order of BNSL. As an example, Figure S4 (Supporting Information) shows that multiple stacking faults in AlB_2-type BNSL did not wash out sharp reciprocal lattice reflections in the FFT power spectra.

3.4.2. Twin Boundaries. Twinning is the oriented association of two domains of the same crystalline phase which are related to each other by some symmetry operation that does not belong to the symmetry of the crystal. Typically, it is a mirror reflection of the lattice across the twin plane.[48] Twinned crystals can form either during growth or as a result of mechanical deformation.[49] An example of the twin boundary in the *fcc* superlattice is shown in Figure S5 (Supporting Information). The occurrence of twin planes is associated with additional twinning energy. In general, twinning is a low-energy defect compared to most other planar defects. For example, in *fcc* crystals the energy associated with the formation of the twin plane is often approximated as one-half of the stacking fault energy.[50] The formation of twin planes can even be energetically favorable during early stages of crystal growth because it allows minimization of the surface area without introducing high-energy facets.[50,51]

We observed examples of twin boundaries in BNSLs with cubic unit cells, such as the $NaZn_{13}$-type lattice based on simple cubic packing of large NCs (Figure 5a). The model of the twinned $NaZn_{13}$ lattice with the (111) twin plane is shown in Figure 4b and is in agreement with experimental TEM images. Figure S6 (Supporting Information) shows twinning in BNSL with the *bcc*-AB_6 structure recently reported by Ye at al.[52] This structure also belongs to the cubic family and has a body-centered cubic sublattice of large NCs. Again, the twin plane was the (111) plane of the *bcc*-AB_6 lattice. In both structures, the twin boundaries formed clean transitions between the crystalline

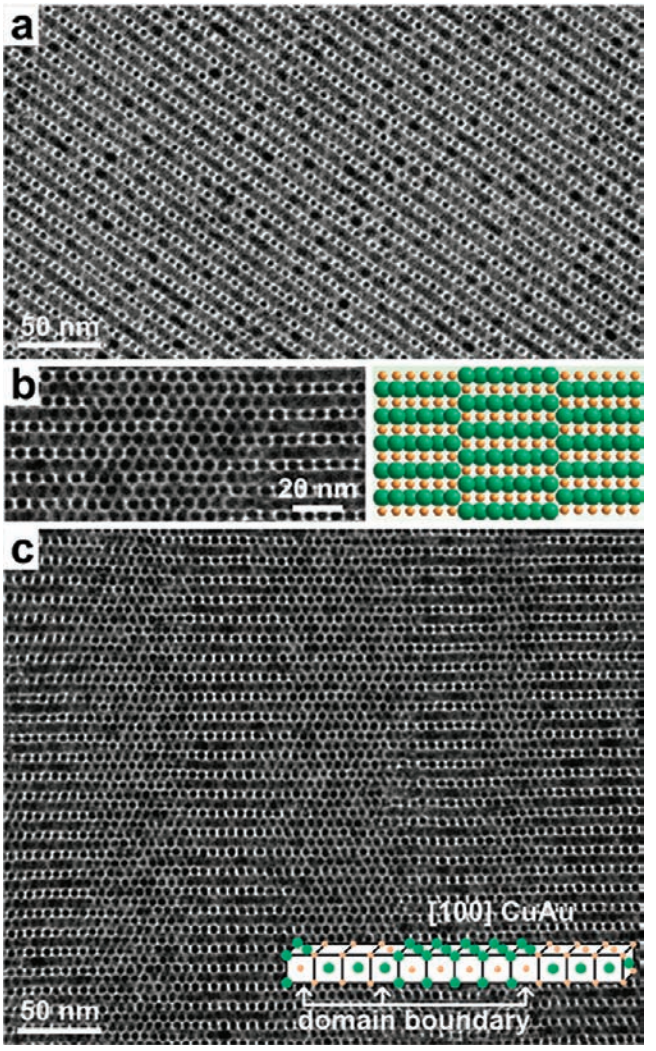

Figure 6. (a) TEM image of [100] projection for CuAu-type BNSL self-assembled at 20 °C from 7.7 nm PbSe and 3.4 nm Pd NCs. (b) TEM image and structural model of the antiphase boundary in CuAu-type BNSL. (c) Periodic antiphase boundaries viewed along the [100] projection of CuAu-type BNSLs self-assembled at 80 °C from 7.7 nm PbSe and 3.4 nm Pd NCs. The inset shows a structural model.

domains. We also observed twin boundaries in the BNSL isostructural with hexagonal $MnZn_2$ Laves phase (Figure S7, Supporting Information).

3.4.3. Antiphase Boundaries. BNSLs isostructural with tetragonal CuAu phase are commonly observed in binary assemblies of NCs, especially at large γ-ratios where the CuAu lattice has a rather high packing density.[14,34] The CuAu-type BNSLs can be recognized by their characteristic [100] projections consisting of well-separated alternating layers of small and large NCs (Figure 6a). This structure can develop an interesting type of defect where NCs interchange their positions in the unit cell on opposite sides of the plane known as the antiphase boundary. At this boundary the CuAu lattice is shifted by $(0, b/2, c/2)$, where b and c are the lattice parameters, along the ⟨001⟩ axis. The antiphase boundaries do not affect orientations of crystallographic axes, but each side of the boundary has an opposite phase: for example, the ordering of the NC layers along the ⟨001⟩ axis changes from ABABABAB in a perfect lattice to BABABABA

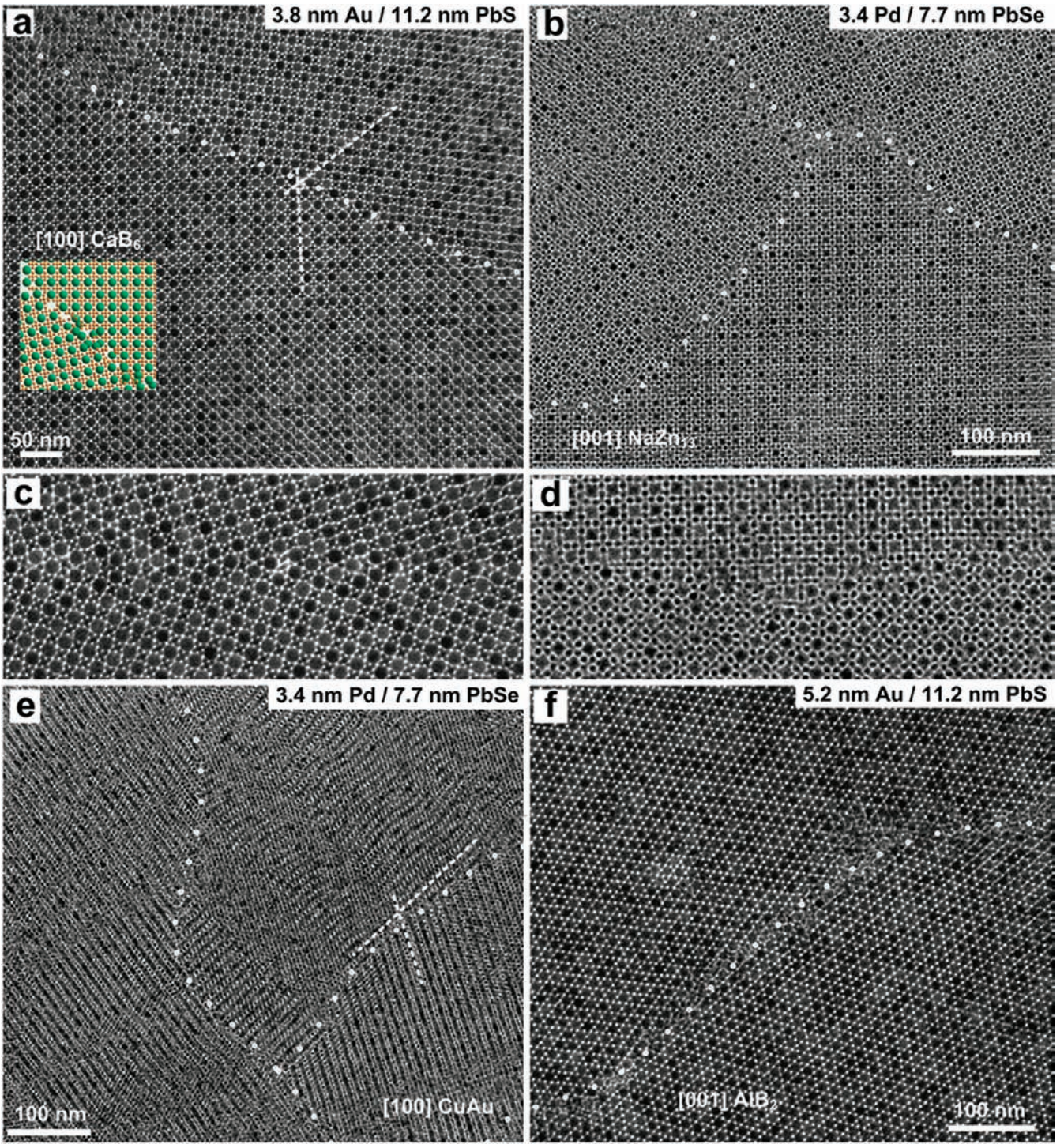

Figure 7. Tilt grain boundaries in BNSLs. TEM images of high-angle tilt boundaries between: (a) [001] oriented domains of CaB_6-type BNSLs self-assembled from 11.2 nm PbS and 3.8 nm Au NCs; (b) [001] oriented domains of $NaZn_{13}$-type BNSLs assembled from 7.7 nm PbSe and 3.4 nm Pd NCs; (c,d) a closer look at the grain boundaries in CaB_6 and $NaZn_{13}$ BNSLs, respectively; (e,f) high-angle tilt grain boundaries between (e) [100] oriented domains of CuAu-type BNSLs formed by 7.7 nm PbSe and 3.4 nm Pd NCs and (f) [001] oriented domains of AlB_2-type BNSLs formed by 11.2 nm PbS and 5.2 nm Au NCs.

on the opposite size of the antiphase boundary. In Figure 6b, the antiphase boundaries are shown for CuAu-type BNSL self-assembled from 7.7 nm PbSe and 3.4 nm Pd NCs.

The antiphase boundaries parallel to the (001) plane have been reported for the CuAu intermetallic compounds.[53] The formation of periodic antiphase boundaries in CuAu atomic alloys becomes thermodynamically favorable in the narrow temperature window immediately below the ordering temperature (380−410 °C).[54,55] We also noticed that periodic antiphase domain boundaries usually formed in CuAu-type BNSLs self-assembled at elevated temperatures between 50 and 80 °C, whereas the BNSLs formed at lower temperatures (−20 to

25 °C) showed very low concentration of antiphase boundaries. The periodic antiphase boundaries in CuAu-type BNSLs self-assembled from 7.7 nm PbSe and 3.4 nm Pd NCs at 80 °C were separated by about five unit cells (Figure 6c), which was in agreement with the observations for the parent CuAu intermetallic compound where periodic antiphase domains were also five unit cells wide.[55] At the same time, we also observed a variable width of antiphase domains in CuAu-type BNSL (Figure S8, Supporting Information).

3.4.4. Grain Boundaries. Twin and antiphase boundaries represent special cases of grain boundaries with a high degree of symmetry between crystal lattices in both grains and with a high degree of fit between the lattices at the interface. These two examples represent a small subset of a much broader class of grain boundaries which connect two domains of the same structure with different orientations of crystallographic axes. A general description of grain boundaries is rather complicated because even a simple boundary requires five independent parameters (degrees of freedom) for accurate description of the orientation of the boundary plane with respect to the lattices in both grains.[56] In many practical cases, however, the description of grain boundaries can be simplified by taking into consideration only the orientational relationship between crystal lattices.[57] The two simplest cases of grain boundaries include tilt and twist boundaries. In the former case, the rotation axis is parallel to the boundary plane, while in twist boundary the rotation axis is normal to the boundary plane. There are also boundaries of mixed type, combining both tilt and twist components.[56]

The energy of a grain boundary depends on the number of broken bonds at the interface. The coincidence site lattice (CSL) theory describes the degree of fit between two grains at the interface by calculating the ratio of coincidence lattice sites to the total number of sites near the interface.[57] This approach allows predicting the grain boundaries with low energy, which would be the most stable and therefore most favorable boundaries in a polycrystalline material. At the same time, it is very difficult to either calculate or measure grain boundary energies in atomic solids. Equally challenging is the reconstruction of the interfacial layer from HRTEM images. A good amount of work has been done for metals with cubic structure where grain boundaries largely determine electrical and thermal conductivity and mechanical properties.[57] At the same time, much less information is available for grain boundaries in solids with complex unit cells. Here, BNSLs provide an extremely useful model system for analysis of boundaries and interfaces.

Grain boundaries are very common in BNSLs. They can form via different mechanisms. First, two BNSL domains can independently nucleate and grow until they contact each other. In this case. it is very unlikely that the entire BNSL domain could change its orientation to provide a better fit between grains. Instead, we should expect local rearrangements of NCs attempting to minimize the interfacial energy for a given (arbitrary) orientation of BNSL domains. Figure 7 shows several examples of tilt grain boundaries formed between domains of CaB_6-type, $NaZn_{13}$-type, CuAu-type, and AlB_2-type BNSLs self-assembled from different NCs. Figure S9 (Supporting Information) shows several other examples of these common defects. All these examples depict grain boundaries with high misorientation angles between the grains. Such high-angle grain boundaries typically result in poor fits between lattices with multiple broken bonds, interstitial atoms, or a thin amorphous layer between the grains (e.g., Figure 7a, inset). All these features can be observed in the tilt boundaries formed between BNSL domains. At the same time, a closer look at the boundaries (Figure 7c,d) shows how complex CaB_6-type and $NaZn_{13}$-type lattices tilted at 36° and 48°, respectively, arrange toward minimization of the interfacial energy.

Among various types of high-angle grain boundaries, there are special types that provide a good fit between atomic lattices of the grains and have relatively low energy. These grain boundaries require precise crystallographic alignment between the grains. It appears improbable that such interfaces formed through coalescence of independently nucleated but perfectly prealigned BNSL domains. Instead, we rather expect that low-energy grain boundaries formed due to an abrupt change of the superlattice growth direction.

Figure 8 shows several examples of (nearly) coherent grain boundaries between BNSL domains. Figures 8a and b show twist boundaries in AlB_2-type BNSLs where the grains are twisted by 90° around the axis normal to the boundary plane. The model shown in Figure 8b provides reconstruction of the interface and is in a good agreement with TEM data. Figure 8c shows an example of the tilt boundary in CaB_6-type BNSL where grains are tilted at a 45° angle with respect to each other. Finally, Figure 8d shows the TEM image of NaCl-type BNSL where the grain viewed as a [001] projection (top) transforms to the grain corresponding to the [211] projection of the NaCl lattice. This transformation cannot be performed by tilting or twisting only but required twisting by 45° followed by a ~35° tilt characteristic of the mixed type of grain boundary.

3.4.5. Phase Boundaries. Different BNSL structures can nucleate and grow simultaneously on the same substrate. The coalescence of two different BNSLs generates the phase boundary, in a similar manner to the formation of grain boundaries. An alternative scenario would imply consecutive growth of two different BNSL phases separated by a phase boundary, in a similar manner to the growth of heterostructures in conventional solids. In the latter case, one can expect the formation of a low-energy boundary or even an epitaxial boundary between two phases. The epitaxial growth can occur between two phases when there is a good fit between lattices on the opposite sides of the phase boundary.

Figure 9 shows several examples of phase boundaries formed between CuAu- and $NaZn_{13}$-type BNSLs, between $NaZn_{13}$- and AlB_2-type BNSLs, and between CuAu- and AlB_2-type BNSLs self-assembled from different combinations of NCs. In most cases, the analysis of the boundary region revealed no epitaxial relationship between different BNSL domains. We therefore proposed that a majority of the phase boundaries observed in our BNSL studies formed through the coalescence of independently nucleated islands, rather than through the consecutive growth of BNSL phases. At the same time, our early work showed one example of an epitaxial boundary between $NaZn_{13}$- and AlB_2-type BNSLs.[14]

3.4.6. What Does the Boundary between a Crystal and a Quasicrystal Look Like? We carried out a systematic study to explore arguably the most intriguing type of phase boundaries, which is the boundary between periodic and aperiodic (quasicrystalline) phases.

The dodecagonal quasicrystalline (DDQC) superlattice has irrational stoichiometry $A_{(2+\sqrt{3})}B_{(4+6\sqrt{3})} \sim AB_{3.86}$ and 12-fold rotational symmetry forbidden in any periodic lattice.[15] This structure can be mapped onto the quasicrystalline square-triangular tiling as described in Section 3.3.3 and shown in Figure 3d. The close proximity of the DDQC phase to "parent" AlB_2- and CaB_6-type BNSLs allows for generation of samples with

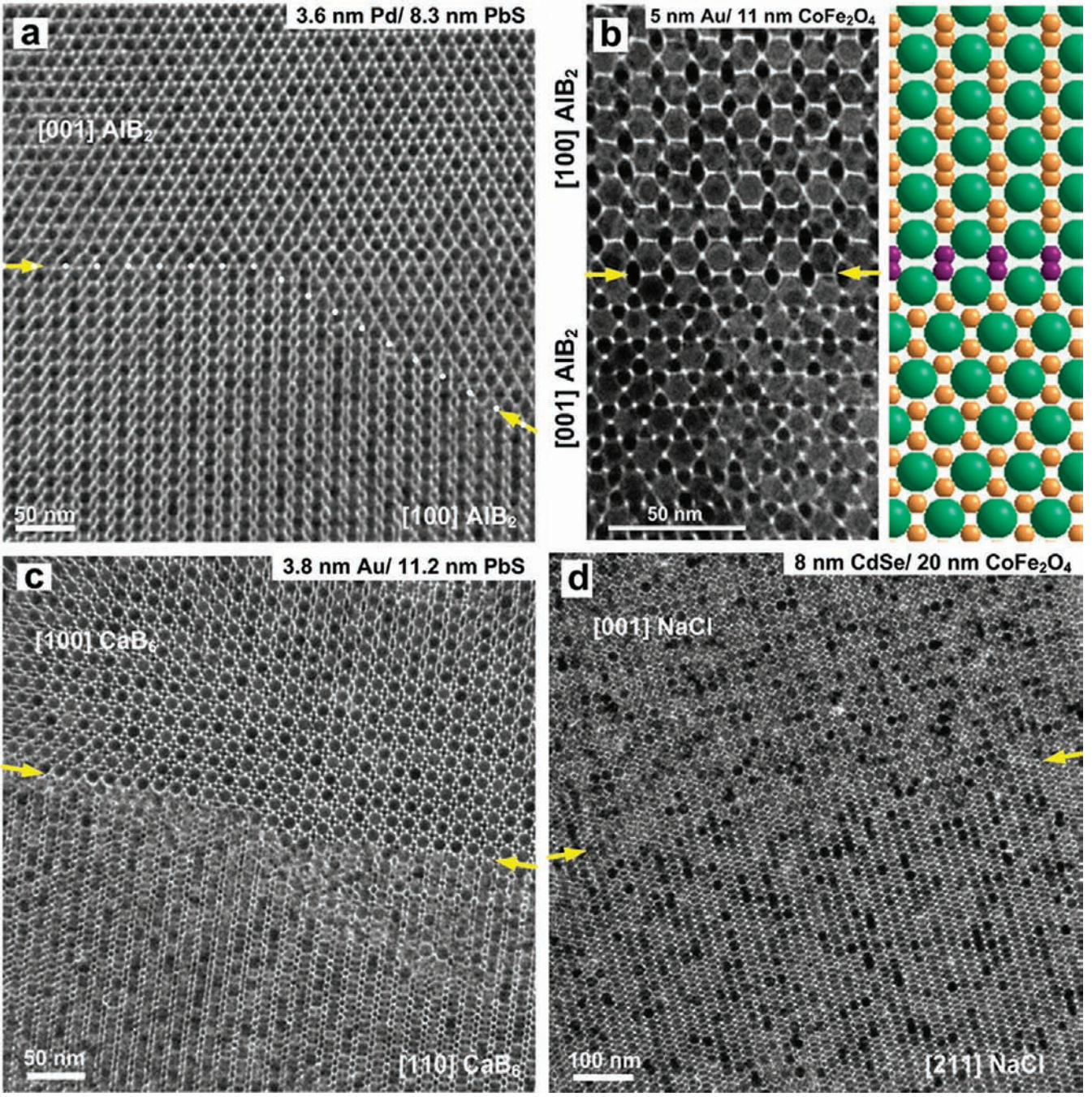

Figure 8. Low-energy grain boundaries in BNSLs. (a) TEM image of 90° twist grain boundary between AlB_2-type BNSL domains. (b) A model of the twist grain boundary in AlB_2-type BNSL compared to the TEM image. (c) 45° tilt grain boundary in CaB_6-type BNSL. (d) A grain boundary in NaCl-type BNSL with lattice domains both tilted and twisted with respect to each other. Yellow arrows highlight the grain boundaries.

DDQC-CaB_6 and DDQC-AlB_2 interfaces simply by shifting NC concentration ratios from the ideal one (1:3.86) to those containing an excess or deficiency of metallic particles, respectively. In the former case, we observed the formation of CaB_6-type BNSLs that often formed rather regular phase boundaries with the DDQC lattice (Figure 10a). Our previous study revealed that boundaries between CaB_6 and DDQC phases often contained a thin "wetting layer" of ($3^3.4^2$) Archimedean tiling (Figure 11b,c).[15] In this work, we found another common structural element associated with the boundary between CaB_6 and DDQC phases. Figure 11a shows a closer look at the boundary which contains four identical clusters of disclinations (Figure 11d). Each cluster of disclinations formed a dislocation[47] that should be conceptually analogous to the misfit dislocations at the phase boundaries between crystalline phases.

Figure 10b shows an example of the boundary between AlB_2 and DDQC phases. These boundaries typically showed a higher degree of disorder compared to the CaB_6−DDQC boundaries. Figure 11e shows a fragment of the AlB_2−DDQC boundary viewed along the [001] projection of the AlB_2 lattice. It shows a relatively smooth transition between AlB_2 and quasiperiodic lattices. Interestingly, the transition from the DDQC phase to

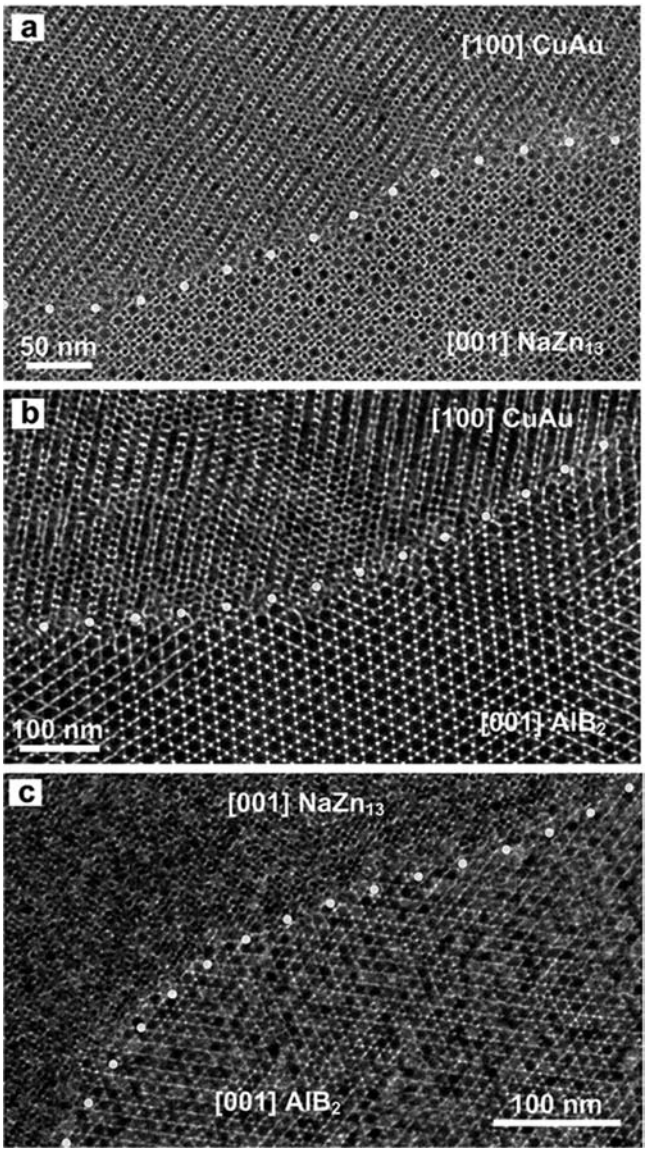

Figure 9. Phase boundaries in BNSLs. (a) CuAu-type BNSL forms a phase boundary with $NaZn_{13}$-type BNSL. Both structures self-assembled from 7.7 nm PbSe and 3.4 nm Pd NCs; (b) phase boundary between AlB_2- and CuAu-type BNSLs self-assembled from 7.7 nm PbSe and 3.4 nm Pd NCs; (c) phase boundary between $NaZn_{13}$- and AlB_2-type BNSLs self-assembled from 10.7 nm PbS and 5.2 nm Au NCs.

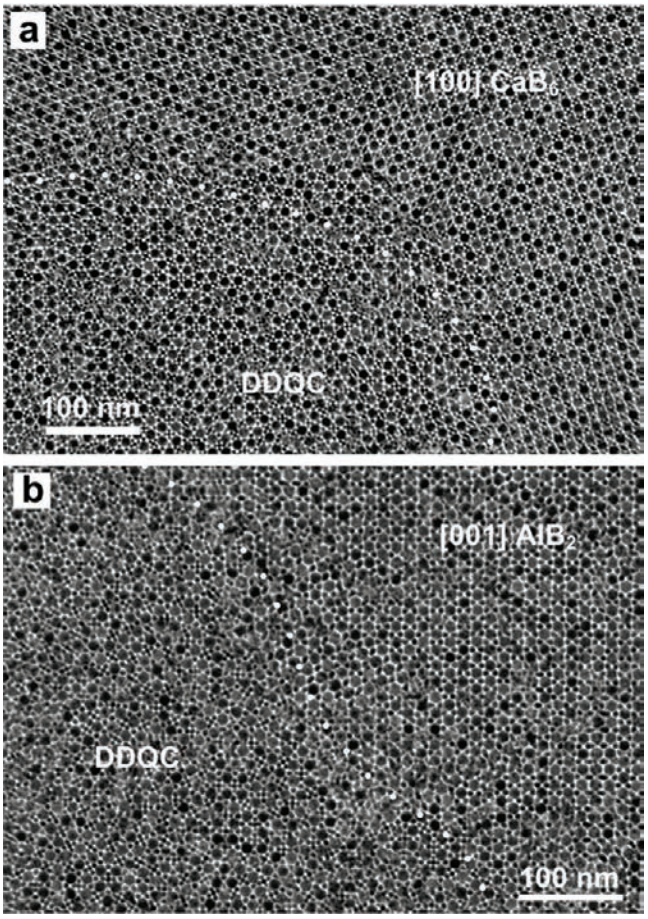

Figure 10. TEM micrographs of phase boundaries between periodic and quasicrystalline phases: (a) phase boundary between the dodecagonal quasicrystalline superlattice and CaB_6-type BNSL self-assembled from 11.2 nm PbS and 3.8 nm Au NCs and (b) phase boundary between dodecagonal quasicrystalline superlattice and AlB_2-type BNSL formed by 11.2 nm PbS and 5.2 nm Au NCs.

AlB_2 BNSL contained square and triangular units arranged into small fragments of $(3^3.4^2)$ Archimedian tiling. Recent studies of Mikhael and Glotzer suggested the unique role of $(3^3.4^2)$ Archimedian tiling as the pseudomorphic phase with both crystalline and quasicrystalline structural features.[58,59] As in the previous case, misfit dislocations could be found in proximity of the phase boundary. The structure of dislocations was identical to that shown in Figure 11d, which probably corresponded to the lowest-energy line defect in the DDQC phase. In the BNSLs self-assembled from 12.6 nm Fe_3O_4 and 4.7 nm Au NCs, we also observed an interesting type of phase boundary between the DDQC phase AlB_2-type BNSL viewed in Figure 11f along the [010] projection.

3.5. Bulk (Three-Dimensional) Defects. Bulk defects include voids, cracks, and precipitates, which are the most severe imperfections in solids. Figure 12 shows the examples of bulk structural defects in BNSLs. The voids in BNSL thin films (Figure 12a) form due to local disruption of BNSL growth. An important point is that void does not disrupt the long-range order of the BNSL. Such void could be templated either by an impurity or by a small gas bubble created during evaporation of a colloidal solution. Voids can also form if the superlattice grows on a rough substrate. At this point we can only speculate about the mechanisms of void formation in BNSLs. On the other hand, the formation of cracks in NC superlattices (Figure 12b) is easy to understand. The surface ligands form soft shells around each NC. These ligands swell in the presence of a good solvent and shrink when solvent is gone or if solvent polarity increases.[60,61] These changes in the effective thickness of the ligands shell can generate strain in BNSLs. Formation of cracks is one of the most common strain release mechanisms.

The third type of bulk defect, precipitate, can form in a number of ways. The formation of precipitates is very likely a result of phase separation between BNSL and excess NCs or some impurities. For example, a growing BNSL structure can encapsulate other NCs. Very often these precipitates are disordered NC aggregates. Sometimes, precipitates can include small superlattice domains. Figure 12c shows such an example where the

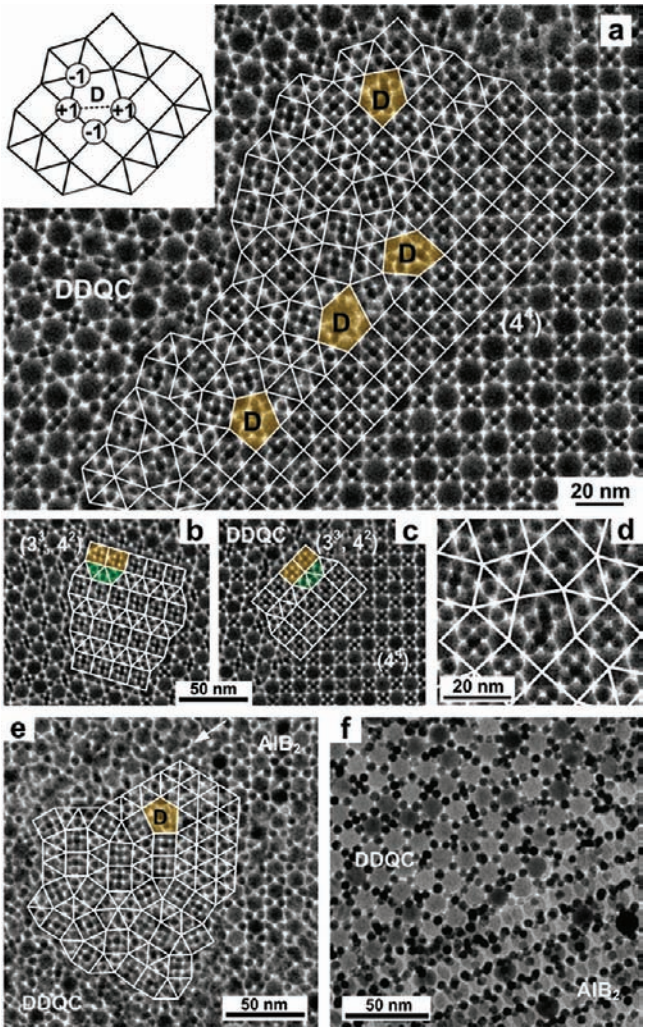

Figure 11. Boundaries between crystalline and quasicrystalline phases. (a) TEM image of the interface between DDQC and CaB_6-type BNSLs. The inset shows the structural defect ("misfit" dislocation) often observed near the interface between crystalline and quasicrystalline phases. (b) TEM image of a BNSL isostructural with $(3^3.4^2)$ Archimedean tiling. (c) TEM image of a boundary between DDQC and CaB_6-type BNSLs with the elements of $(3^3.4^2)$ Archimedian tiling as the "wetting" layer. (d) An enlarged view of characteristic dislocation formed at the boundary between DDQC and CaB_6-type BNSLs. All structures in (a−d) self-assembled from 11.2 nm PbS and 3.8 nm Au NCs. (e) TEM image of the interface between DDQC and AlB_2-type BNSLs self-assembled from 11.2 nm PbS and 5.2 nm Au NCs. One can see the elements of $(3^3.4^2)$ Archimedian tiling at the boundary. The arrow highlights the stacking fault in the AlB_2 lattice. (f) A phase boundary formed between DDQC and AlB_2-type BNSLs self-assembled from 13.4 nm Fe_2O_3 and 5 nm Au NCs.

precipitate formed inside a CaB_6-type BNSL contained a tilted domain of the same BNSL structure and a small inclusion of the DDQC superlattice.

3.6. Structural Defects Originating from the Size Dispersion of Nanocrystals. In addition to structural defects that have direct analogues in atomic crystals, BNSLs can generate their own, unique defects that cannot exist in atomic or molecular structures. The important difference between atoms and NCs is the finite size distribution of NCs. An example of this effect is shown in Figure 13 where CuAu-type BNSL self-assembled from

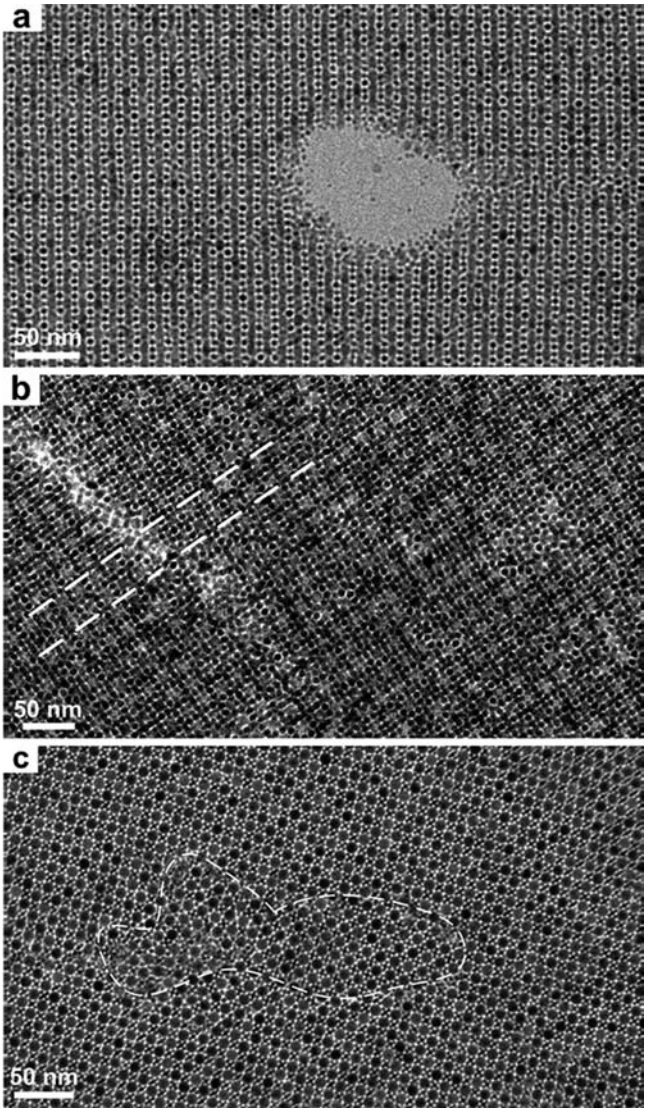

Figure 12. TEM images of bulk (three-dimensional) defects in BNSLs. (a) Void in CuAu-type BNSL self-assembled from 7.7 nm PbSe and 3.4 nm Pd NCs. (b) Crack in $NaZn_{13}$-type BNSL assembled from 11.2 nm PbS and 7 nm Au NCs. The lattice fringes remain aligned on both sides of the crack. (c) Crystalline precipitate in CaB_6-type BNSL self-assembled from 11.2 nm PbS and 3.8 nm Au NCs.

rather monodisperse 11 nm $CoFe_2O_4$ NCs and polydisperse Au NCs with sizes varied from 4.3 to 6.0 nm (see Figure S10, Supporting Information, for size histograms). This binary lattice formed despite obvious polydispersity of the building blocks. Previous experimental and theoretical studies for single-component hard sphere colloids reported suppression of crystallization if polydispersity of the colloidal particles exceeded 10−12%.[62,63] Figure 13 shows that BNSLs can easily circumvent this limitation. One possible explanation is that soft shells of surface ligands around NCs smoothen the variations in the diameter of the inorganic NC cores. Such local compensations work well at the level of random inclusions of small and large NCs. At the same time, surface ligands cannot help when multiple large (or small) NCs integrate into BNSL in close proximity to each other. In that case, to compensate for local variations in the lattice constant, BNSLs generate a new type of structural defect that can be called

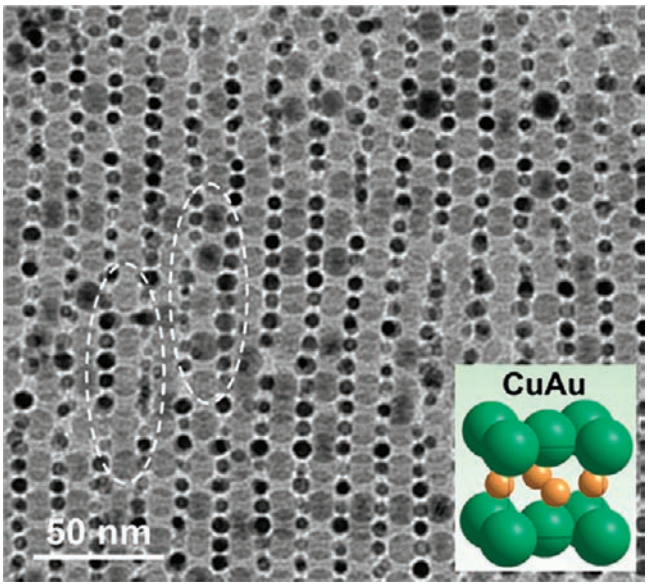

Figure 13. An example of BNSL self-assembled from monodisperse 11 nm $CoFe_2O_4$ NCs and polydisperse (4.3−6.9 nm) Au NCs. Dashed lines highlight the "antiwave" defects, where the size of Au NCs in adjacent rows varies in opposite ways to maintain the lattice constant and to reduce lattice strain.

"antiwave" defect. The size of Au NCs in the neighboring rows of unit cells changes inversely proportional to each other. When large NCs occupied several unit cells in the same row, the unit cells in the adjacent row contained the NCs with size smaller than the average NC size, as seen in the [100] projection of CuAu-type BNSL shown in Figure 13. The formation of these defects is probably driven by the lattice strain.

4. CONCLUSIONS

This work represents the first attempt to systematically analyze structural defects in BNSLs. We found many similarities in the crystallography of defects in atomic lattices and BNSLs, suggesting similar mechanisms of defect formation in both types of solids. In addition, new types of defects emerge in BNSLs caused by size variation of BNSL building blocks. The ability to observe these defects using routine electron microscopy offers existing opportunities for detailed structural analysis of defects in complex binary lattices. Moreover, BNSLs allow simultaneous observation of multiple lattice defects and provide a general platform to study interactions between different defects. Figure S11 (Supporting Information) shows such an example of AlB_2-type BNSLs incorporating different defects: vacancies, dislocations, disclinations, stacking faults, voids, and precipitates. Analysis of such images allows for the study of nonobvious relations between various types of structural defects.

Rapid development of electron microscopy techniques will further broaden the utility of BNSLs as the test bed for structural analysis of solids. For example, in situ TEM[64] may allow the observation of lattice dynamics in the real space and real time. Growing BNSLs on curved substrates should address many open questions in nonplanar crystallography.[65,66] These are only a few random examples focusing on the crystallography problems. The ultimate goal for such studies is to create novel practical materials self-assembled from functional building blocks.

■ ASSOCIATED CONTENT

Supporting Information. Additional experimental details and TEM images. This material is available free of charge via the Internet at http://pubs.acs.org.

■ AUTHOR INFORMATION

Corresponding Author
dvtalapin@uchicago.edu

■ ACKNOWLEDGMENT

We thank S. M. Rupich for synthesis of PbS and PbSe NCs, M. V. Kovalenko for synthesis of CdSe NCs, W. Irving and S. Rice for stimulating discussions, and M. Boles for careful reading of the manuscript. The work was jointly funded by the NSF MRSEC Program under Award Number DMR-0213745 and by the Office of Naval Research under Award Number N00014-10-1-0190. We acknowledge infrastructure support by the NSF Center of Energetic Non-Equilibrium Chemistry at Interfaces (CENECI). D.V.T. also thanks the David and Lucile Packard Foundation. The work at the Center for Nanoscale Materials (ANL) was supported by the U.S Department of Energy under Contract No. DE-AC02-06CH11357.

■ REFERENCES

(1) Talapin, D. V.; Lee, J. S.; Kovalenko, M. V.; Shevchenko, E. V. *Chem. Rev.* **2010**, *110*, 389–458.
(2) Murray, C. B.; Kagan, C. R.; Bawendi, M. G. *Ann. Rev. Mater. Sci.* **2000**, *30*, 545–610.
(3) Zeng, H.; Sun, S. H. *Adv. Funct. Mater.* **2008**, *18*, 391–400.
(4) Murray, C. B.; Kagan, C. R.; Bawendi, M. G. *Science* **1995**, *270*, 1335–1338.
(5) Bodnarchuk, M. I.; Kovalenko, M. V.; Pichler, S.; Fritz-Popovski, G.; Hesser, G.; Heiss, W. *ACS Nano* **2010**, *4*, 423–431.
(6) Redl, F. X.; Cho, K. S.; Murray, C. B.; O'Brien, S. *Nature* **2003**, *423*, 968–971.
(7) Shevchenko, E. V.; Talapin, D. V.; Kotov, N. A.; O'Brien, S.; Murray, C. B. *Nature* **2006**, *439*, 55–59.
(8) Dong, A. G.; Chen, J.; Vora, P. M.; Kikkawa, J. M.; Murray, C. B. *Nature* **2010**, *466*, 474–477.
(9) Chen, Z.; O'Brien, S. *ACS Nano* **2008**, *2*, 1219–1229.
(10) Kovalenko, M. V.; Bodnarchuk, M. I.; Talapin, D. V. *J. Am. Chem. Soc.* **2010**, *132*, 15124–15126.
(11) Evers, W. H.; Friedrich, H.; Filion, L.; Dijkstra, M.; Vanmaekelbergh, D. *Angew. Chem., Int. Ed.* **2009**, *48*, 9655–9657.
(12) Dong, A.; Ye, X.; Chen, J.; Murray, C. B. *Nano Lett.* **2011**, *11*, 1804–1809.
(13) Talapin, D. V.; Shevchenko, E. V.; Murray, C. B.; Titov, A. V.; Kral, P. *Nano Lett.* **2007**, *7*, 1213–1219.
(14) Shevchenko, E. V.; Talapin, D. V.; Murray, C. B.; O'Brien, S. *J. Am. Chem. Soc.* **2006**, *128*, 3620–3637.
(15) Talapin, D. V.; Shevchenko, E. V.; Bodnarchuk, M. I.; Ye, X. C.; Chen, J.; Murray, C. B. *Nature* **2009**, *461*, 964–967.
(16) Bigioni, T. P.; Lin, X.-M.; Nguyen, T. T.; Corwin, E. I.; Witten, T. A.; Jaeger, H. M. *Nat. Mater.* **2006**, *5*, 265–270.
(17) Friedrich, H.; Gommes, C. J.; Overgaag, K.; Meeldijk, J. D.; Evers, W. H.; Nijs, B. d.; Boneschanscher, M. P.; de Jongh, P. E.; Verkleij, A. J.; de Jong, K. P.; van Blaaderen, A.; Vanmaekelbergh, D. *Nano Lett.* **2009**, *9*, 2719–2724.
(18) Rupich, S. M.; Shevchenko, E. V.; Bodnarchuk, M. I.; Lee, B.; Talapin, D. V. *J. Am. Chem. Soc.* **2010**, *132*, 289–296.
(19) Nagel, M.; Hickey, S. G.; Fromsdorf, A.; Kornowski, A.; Weller, H. *Z. Phys. Chem.* **2007**, *221*, 427–437.

(20) Shevchenko, E.; Talapin, D.; Kornowski, A.; Wiekhorst, F.; Kotzler, J.; Haase, M.; Rogach, A.; Weller, H. *Adv. Mater.* **2002**, *14*, 287–290.
(21) Talapin, D. V.; Shevchenko, E. V.; Kornowski, A.; Gaponik, N.; Haase, M.; Rogach, A. L.; Weller, H. *Adv. Mater.* **2001**, *13*, 1868–1871.
(22) Bodnarchuk, M. I.; Li, L.; Fok, A.; Nachtergaele, S.; Ismagilov, R. F.; Talapin, D. V. *J. Am. Chem. Soc.* **2011**, *133*, 8956–8960.
(23) Chen, J.; Ye, X.; Murray, C. B. *ACS Nano* **2010**, *4*, 2374–2381.
(24) Schall, P.; Cohen, I.; Weitz, D. A.; Spaepen, F. *Science* **2004**, *305*, 1944–1948.
(25) Schall, P.; Cohen, I.; Weitz, D. A.; Spaepen, F. *Nature* **2006**, *440*, 319–323.
(26) Wang, Z. L. *Adv. Mater.* **1998**, *10*, 13–30.
(27) Hines, M. A.; Scholes, G. D. *Adv. Mater.* **2003**, *15*, 1844–1849.
(28) Talapin, D. V.; Murray, C. B. *Science* **2005**, *310*, 86–89.
(29) Talapin, D. V.; Rogach, A. L.; Kornowski, A.; Haase, M.; Weller, H. *Nano Lett.* **2001**, *1*, 207–211.
(30) Bodnarchuk, M. I.; Kovalenko, M. V.; Groiss, H.; Resel, R.; Reissner, M.; Hesser, G.; Lechner, R. T.; Steiner, W.; Schaffler, F.; Heiss, W. *Small* **2009**, *5*, 2247–2252.
(31) Kovalenko, M. V.; Bodnarchuk, M. I.; Lechner, R. T.; Hesser, G.; Schaffler, F.; Heiss, W. *J. Am. Chem. Soc.* **2007**, *129*, 6352–6353.
(32) Prasad, B. L. V.; Stoeva, S. I.; Sorensen, C. M.; Klabunde, K. J. *Langmuir* **2002**, *18*, 7515–7520.
(33) Peng, S.; Lee, Y. M.; Wang, C.; Yin, H. F.; Dai, S.; Sun, S. H. *Nano Res.* **2008**, *1*, 229–234.
(34) Bodnarchuk, M. I.; Kovalenko, M. V.; Heiss, W.; Talapin, D. V. *J. Am. Chem. Soc.* **2010**, *132*, 11967–11977.
(35) Leunissen, M. E.; Christova, C. G.; Hynninen, A.-P.; Royall, C. P.; Campbell, A. I.; Imhof, A.; Dijkstra, M.; van Roij, R.; van Blaaderen, A. *Nature* **2005**, *437*, 235–240.
(36) Ohara, P. C.; Leff, D. V.; Heath, J. R.; Gelbart, W. M. *Phys. Rev. Lett.* **1995**, *75*, 3466.
(37) Bishop, K. J. M.; Wilmer, C. E.; Soh, S.; Grzybowski, B. A. *Small* **2009**, *5*, 1600–1630.
(38) van Bueren, H. G. *Imperfections in crystals*; North-Holland Publishing Company: Amsterdam, 1960.
(39) Mariani, D. F.; Decastro, M. J.; Rivas, J. L. A. *J. Phys.: Condens. Matter* **1994**, *6*, 945.
(40) Kornblit, L. *Phys. Status Solidi (b)* **1983**, *115*, 485–491.
(41) Johnson, R. A. *J. Phys. F: Met. Phys.* **1973**, *3*, 295–321.
(42) Hull, D.; Bacon, D. J. *Introduction to Dislocations*, 4th ed.; Oxford: Oxford, 2001; Vol. Butterworth-Heinemann.
(43) Glaser, M. A.; Clark, N. A. In *Advances in Chemical Physics*; John Wiley & Sons, Inc.: Hoboken, USA, 2007; pp 543−709.
(44) Kleman, M. *Points, lines and walls: in liquid crystals, magnetic systems and various ordered media*; Wiley-Interscience: Manchester, 1983.
(45) Widom, M. *Phys. Rev. Lett.* **1993**, *70*, 2094–2097.
(46) Oxborrow, M.; Henley, C. L. *Phys. Rev. B* **1993**, *48*, 6966–6998.
(47) Leung, P. W.; Henley, C. L.; Chester, G. V. *Phys. Rev. B* **1989**, *39*, 446.
(48) Yong, K.-T.; Sahoo, Y.; Swihart, M. T.; Prasad, P. N. *J. Phys. Chem. C* **2007**, *111*, 2447–2458.
(49) Kelly, A.; Groves, G. W. *Crystallography and crystal defects*; Addison-Wesley publishing company: London, 1970.
(50) Howie, A.; Marks, L. D. *Philos. Mag. A.* **1984**, *49*, 95–109.
(51) Marks, L. D. *Philos. Mag. A.* **1984**, *49*, 81–93.
(52) Ye, X.; Chen, J.; Murray, C. B. *J. Am. Chem. Soc.* **2011**, *133*, 2613–2620.
(53) Glossop, A. B.; Pashley, D. W. *Proc. R. Soc. London A* **1959**, *250*, 132–146.
(54) Barret, C.; Massalski, T. B. *Structure of metals*, 3rd ed.; Pergamon Press: New York, 1987.
(55) Watanabe, D.; Takashima, K. *J. Appl. Crystallogr.* **1975**, *8*, 598–602.
(56) Bollmann, W. *Crystal Defects and Crystalline Interfaces*; Springer-Verlag: Berlin-Heidelberg-New-York, 1970.
(57) Sutton, A.; Balluffi, R. *Interfaces in Crystalline Materials*; Oxford University Press: Oxford, 1996.
(58) Mikhael, J.; Roth, J.; Helden, L.; Bechinger, C. *Nature* **2008**, *454*, 501–504.
(59) Glotzer, S. C.; Keys, A. S. *Nature* **2008**, *454*, 420–421.
(60) Schapotschnikow, P.; Pool, R.; Vlugt, T. J. H. *Nano Lett.* **2008**, *8*, 2930–2934.
(61) Landman, U.; Luedtke, W. D. *Faraday Discuss* **2003**, *125*, 1–22.
(62) Auer, S.; Frenkel, D. *Nature* **2001**, *413*, 711–713.
(63) Kofke, D. A.; Bolhuis, P. G. *Phys. Rev. E* **1999**, *59*, 618.
(64) Zheng, H.; Smith, R. K.; Jun, Y.-w.; Kisielowski, C.; Dahmen, U.; Alivisatos, A. P. *Science* **2009**, *324*, 1309–1312.
(65) Bausch, A. R.; Bowick, M. J.; Cacciuto, A.; Dinsmore, A. D.; Hsu, M. F.; Nelson, D. R.; Nikolaides, M. G.; Travesset, A.; Weitz, D. A. *Science* **2003**, *299*, 1716–1718.
(66) Irvine, W. T. M.; Vitelli, V.; Chaikin, P. M. *Nature* **2010**, *468*, 947–951.